Implications of the DFT+U method on polaron properties in energy materials

Zi Wang, Casey Brock, Amina Matt, and Kirk H. Bevan

Phys. Rev. B **96**, 125150 — Published 26 September 2017

DOI: 10.1103/PhysRevB.96.125150

Implications of the DFT+U method on polaron properties in energy materials

Zi Wang,[1] Casey Brock,[2] Amina Matt,[3] and Kirk H. Bevan[1]
[1] *Materials Engineering, McGill University, Montréal, Québec, H3A 0C5, Canada*[*]
[2] *Materials Science, Vanderbilt University, Nashville, TN 37235, USA*
[3] *Institute of Materials, École polytechnique fédérale de Lausanne, 1015 Lausanne, Switzerland*

To model polaronic behavior in strongly correlated transition metal oxides with *ab initio* methods, one typically requires a level of theory beyond that of local density or general gradient density functional theory (DFT) approximations to account for the strongly correlated d-shell interactions of transition metal oxides. In the present work, we utilize density functional theory with additional on-site Hubbard corrections (DFT+U) to calculate polaronic properties in two lithium ion battery cathode materials, Li_xFePO_4 and $Li_xMn_2O_4$, and two photocatalytic materials, TiO_2 and Fe_2O_3. We investigate the effects of the $+U$ on-site projection on polaronic properties. Through systematic comparison with hybrid functional calculations, it is shown that $+U$ projection in these model materials can impact upon the band gap, polaronic hopping barrier, and polaronic eigenstate offset from the band edges in a non-trivial manner. These properties are shown to have varying degrees of coupling and dependence on the $+U$ projection in each example material studied, which has important implications for arriving at systematic material predictions of polaronic properties in transition metal oxides.

I. INTRODUCTION

Many novel materials used in clean energy applications such as lithium ion batteries[1], photovoltaics[2], and catalysts[3] are transition metal oxides (TMO) and are known to exhibit polaronic behavior[4]. In many such TMOs, the strongly correlated interactions of the d shell electrons open a gap and localize d state conduction electrons into atomic-like orbitals. The localized spatial distribution of these electrons leads to further self trapping through interaction with the surrounding lattice, turning them into polaronic states. Typical local density approximations and generalized gradient approximations (LDA and GGA) calculations greatly underestimate these correlation effects[5,6] leading not only to incorrect predictions for the band gap[7], but also an inability to form polarons on transition metal (TM) sites that arise from these strongly correlated interactions[8]. As such, we require additional corrections to account for these deficiencies in standard LDA/GGA to accurately study polaronic behavior in TMOs. Therefore, in order to further our understanding of such materials for existing and future energy applications, we should strive to accurately model this polaronic behavior.

Density functional theory with on-site Hubbard corrections (DFT+U)[9–11] is widely used to calculate the electronic properties of, amongst other materials, transition metal oxides where correlation plays a large role in its electronic structure. The missing correlation effects in standard LDA/GGA are accounted for by adding an on-site Coulomb repulsion term to specific projected atomic orbitals. Typically, the value of U is either chosen to match an experimental property such as the band gap[7], or obtained from constrained LDA/GGA calculations[12,13]. Additionally, this value of U should also correct for the self interaction error (SIE) typical of semilocal LDA/GGA functionals by restoring piecewise linearity of the total energy as a function of fractional occupation.[14,15]. Coupled with plane wave pseudopotential formalisms, most notably the highly popular projector augmented wave (PAW)[16,17] method, DFT+U has been highly successful in reproducing many properties of such correlated materials at minimal added computational cost. While in principle, DFT+U may add a single parameter to an otherwise *ab initio* calculation in much the same spirit as the fraction α of exact exchange in hybrid functionals[18], its local orbital dependent functional necessitates further parameters, most notably the projection radius, when transforming to on-site atomic orbitals. It has been shown before that this projection radius can significantly affect the system, especially in self-consistent calculations of U[13,19–23]. Effects on localized electronic properties such as polaronic properties are less well studied.

In the PAW formalism, the DFT+U projection radius is conveniently equated to the augmentation radius (r_{PAW})[19]. Typically, there are multiple ways to construct a PAW potential depending on how many semicore electrons are included in the valence, and it is physically justified for the PAW core radius to also vary based on the valency (more electrons in the core lead to a larger core radius). In principle, one would always use a small core PAW potential with semicore electrons included in the valence for higher precision, although this incurs a computational cost from the additional electrons and larger basis set. However, the DFT+U projection radius changes as well, impacting electronic properties that are dependent on the U-term. This makes the choice of U more ambiguous[13,19–23].

In this work, we investigate the effects of DFT+U projection radius and semicore electrons on TM-centered polarons in a set of energy materials that are known to exhibit polaronic behavior and focus on polaronic properties in these materials as illustrated in Fig. 1. The materials studied are rutile TiO_2, Fe_2O_3 (hematite), $LiFePO_4$ and its delithiated form $FePO_4$, and spinel MnO_2. TiO_2

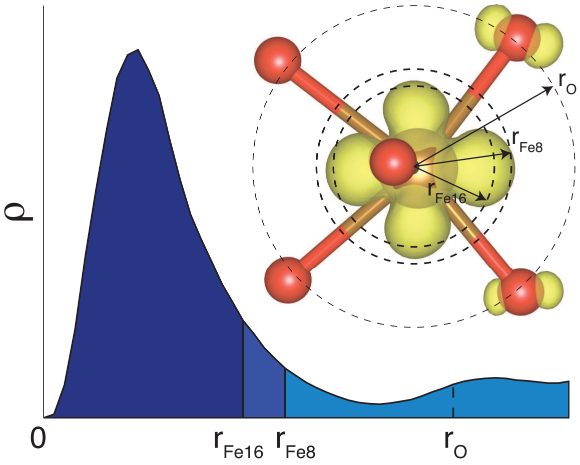

FIG. 1. (Color online) Schematic of the radial charge density distribution (ρ) of a polaronic state taken from Fe_2O_3, centered at the TM site on which the polaron is localized. r_O is the average metal-oxygen bond length, while in this example, r_{Fe8} and r_{Fe16} correspond to two different cutoff radii (r_{PAW}) of a large core Fe potential ($r_{\text{PAW}} = 2.3\ a_0$) with 8 valence electrons, and a small core Fe potential ($r_{\text{PAW}} = 1.9\ a_0$) with 16 valence electrons, respectively. These are also drawn approximately on the MO_6 octahedral complex, which is cut out from the Fe_2O_3 solid. Other materials show similar behavior.

and Fe_2O_3 are materials considered for photocatalytic applications[2,24], while Li_xFePO_4 and $Li_xMn_2O_4$ are utilized within current and next generation lithium ion batteries[1,25].

Our previous DFT+U work on $FePO_4$ has shown that the choice of PAW potential significantly affected the calculated polaron activation energy[26]. Here, not only do we study additional materials, we also include additional comparative HSE06 calculations[6,18,27]. We can separate the contributions from the projection radius and semicore electrons by comparing the results of both DFT+U and HSE06 methods, as the exact exchange is calculated everywhere in HSE06 calculations as opposed to the local U-term which acts only within the projection radius in DFT+U calculations. By conducting such a comprehensive study, we hope to establish a precedent on how to approach polaronic calculations in such a way that consistent results and predictions become more attainable.

II. THEORY

The implementation of DFT+U that we use is a simplified, first order approximation[28] to the general formulation[9–11], and adds a term to the total energy as follows[28]:

$$E_{\text{DFT+U}} = E_{\text{DFT}} + \frac{U_{\text{eff}}}{2} \sum_{t,\sigma} \left(\sum_m n^{t,\sigma}_{m,m} - \sum_{m,m'} n^{t,\sigma}_{m,m'} \, n^{t,\sigma}_{m',m} \right) \tag{1}$$

where the sum of the orbital-projected density matrices (DM) $n^{t,\sigma}_{m,m'}$ is taken over spins σ and atomic sites t. This description depends only on $U_{\text{eff}} \equiv U - J$ and combines the screened Coulomb U and exchange J terms into a single effective parameter U_{eff}. We will label this as just U for the remainder of the work and equate J to 0. It can be shown[29] that this term effects a separation between the occupied and unoccupied one-electron energy levels of the on-site orbitals according to

$$\epsilon^l_{\text{DFT+U}}(N) = \epsilon^l_{\text{DFT}}(N) \pm \frac{U}{2}, \tag{2}$$

where $N = \sum n_i$ is the total number of on-site electrons with angular momentum l (e.g. the d electrons for transition metals) and the sign corresponding to a one-electron energy level increase for unoccupied levels and an energy level decrease for occupied levels with angular momentum l. This localization effect can also be deduced from the form of Eq. (1), which is quadratic in occupancy and favors idempotency of the on-site occupancy matrix $n^{t,\sigma}_{m,m'}$, as the U-term will then be minimized (zero). If the system is Mott-Hubbard (MH) like, the result will be an opening or widening of the d-d band gap. If the system is more charge-transfer (CT) like, the effect will not be as strong, since one band edge (typically the p-hybridized valence band) will not be affected by this d-d split.

The on-site density matrix $n^{t,\sigma}_{m,m'}$ is calculated from a projection of the crystal wave function Ψ onto a set of local orbitals where the on-site coulomb repulsion is expected to take place (typically the d or f orbitals)[19,30,31]:

$$n^{t,\sigma}_{m,m'} = \sum_{n,\mathbf{k}} f^{\sigma}_{n,\mathbf{k}} \left\langle \Psi^{\sigma}_{n,\mathbf{k}} | P^t_{m,m'} | \Psi^{\sigma}_{n,\mathbf{k}} \right\rangle, \tag{3}$$

where $f^{\sigma}_{n,\mathbf{k}}$ is the Fermi distribution. The projection operators $P^t_{m,m'}$ are defined as[19,30,31]

$$P^t_{m,m'}(\mathbf{r},\mathbf{r}') = \theta_{\Omega_t}(\mathbf{r}) \delta \left(|\mathbf{r}' - \mathbf{R}_t| - |\mathbf{r} - \mathbf{R}_t| \right) Y_{l,m}(\hat{\mathbf{r}}) Y^*_{l,m'}(\hat{\mathbf{r}}'), \tag{4}$$

where $Y_{l,m}(\widehat{\mathbf{r} - \mathbf{R_t}})$ is the spherical harmonic of the specific orbital (typically d or f), and $\theta_{\Omega_t}(\mathbf{r})$ is 1 for $|\mathbf{r} - \mathbf{R_t}| < r^t_c$ and zero everywhere else. Crucially, this step function $\theta_{\Omega_t}(\mathbf{r})$ is a hard cutoff determined by r^t_c, which in the PAW formalism is equal to the PAW augmentation radius r_{PAW}[19,31]. Typical PAW augmentation radii for $3d$ transition metals (TM) range from 1.9 a_0 to 2.8 a_0[16] and usually follow the same trend as the elements' ionic radii (decreasing with increasing element number), but can also be modified by inclusion or exclusion of semicore electrons. The $3d$ atomic orbitals tend to have a peak near $r = a_0$, however their tails can fall off rather slowly. Therefore, for example in the case of Fe, a r_{PAW} of 1.9 a_0 for a potential with 16 valence electrons could result in a significantly different projected occupation compared to a r_{PAW} of 2.3 a_0 for a potential with 8 electrons. As the energy term is quadratically dependent on this projection, we believe that this warrants further investigation.

Naturally, the main question of any DFT+U implementation is determining a value of U that is appropriate for the particular system being studied. In theory, this is a single parameter (two if the screened exchange term J is included in higher order implementations[9–11]); but as shown previously, the implementation of a local orbital dependent functional necessitates further parameters that are mostly numerical in nature. In our case, this additional parameter would be the projection radius r_{PAW}. As shown before in previous studies[13,19–23], the dependence on other parameters leads to ambiguities when utilizing constrained DFT techniques[12,13] to self-consistently calculate a value for U, as the resulting value was shown to vary greatly depending on both the projection radius and the basis set used. These ambiguities therefore lend more credence to the contrasting viewpoint of U as an empirical parameter that we can use to fit experimentally measured properties[7,20,21,32], most commonly the band gap. Apart from the band gap, there are of course many other quantities that we can fit U to match, with examples being unit cell volumes/bulk moduli, reaction enthalpies, and polaronic properties such as the location of the polaronic gap state within the band gap.

To put the choice of U on a more fundamental footing, we point out one property of an exact density functional: the piecewise linearity of the total energy as a function of fractional occupation.[14,15]. This linearity is lost in semilocal LDA/GGA[33] due to self interaction errors and results in the favoring of charge delocalization. The DFT+U method works to correct this SIE and restore piecewise linearity, provided that the value for U is consistent. Hybrid functionals provide a similar SIE correction with a consistent value for α. Polaronic systems provide a convenient way to verify this criterion of linearity as we can vary the fractional charge on a polaronic site in a straightforward manner[33–37]. The introduction of the projection radius as a secondary parameter raises the question of whether this influences linearity in addition to the value of the main parameter (be it U or α).

Hybrid functionals[18,27] could be seen as more versatile and consistent as the fraction of exact exchange α is less system dependent and applies to all orbitals as opposed to DFT+U which only treats a selected on-site orbital. This allows for treatment of correlation effects in orbitals that are more hybridized and do not project adequately onto pure atomic states[38] as well as an “occupancy agnostic” treatment for systems that are more CT-like such as $\mathrm{TiO_2}$[39]. This is in contrast to DFT+U, where the effect of the functional and hence the value for U depends on the occupancy of the on-site orbital[13]. These advantages are at the expense of a one to two orders of magnitude increase in computational effort required.

Analogous to the DFT+U method, hybrid functionals rely on a single parameter α which is the fraction of exact exchange that is mixed together with the LSDA/GGA semilocal exchange energy. The effect on strongly correlated materials can be seen as an effective “U-term” acting indiscriminately on all orbitals, both local and non-local[18]. On one hand this can be seen as more elegant and closer to the spirit of *ab initio* calculations, requiring a single parameter that is typically set at a system independent value (typically 25% for the PBE0 functional[6] and its screened variant HSE06[27]), but on the other hand it is not a perfect functional, and there are systems where the higher tunability of DFT+U leads to results that are in better agreement with experiments, an example of which (hematite) will be further investigated in this study. A link between DFT+U and hybrid functionals, as the projected on-site part of the exact exchange has been shown earlier[40]. In this work, we mainly utilize the HSE06 functional as a means to circumvent the dependence on r_{PAW} as both local and non-local exact exchange are treated equally, so we can study the influence of semicore electrons as an independent variable. Assuming that these effects are comparable in DFT+U and subtracting them from our DFT+U results, we can then in turn study solely the effects of changing r_{PAW} in DFT+U.

III. METHOD

All calculations were done in the Vienna Ab-initio Software Package (VASP)[41] using the PBE-GGA semilocal functional[42] within the PAW formalism[16,17]. We utilized this package for our study because its PAW potentials are generally the most utilized by the *ab initio* strongly correlated electronic structure community. However, the general trends explored should be applicable to all DFT+U implementations. Correlations were treated with both DFT+U[10,19,31] and HSE06[18,27] methods. The set of PAW potentials[16] studied was provided and included within VASP. All ionic positions were relaxed until interatomic forces were smaller than 0.005 eV / Å for volume and intrinsic structure calculations, and 0.01 eV / Å for polaron supercell calculations. To form a polaron we added an extra electron to the supercell (compensated by a uniform opposite background charge to maintain charge neutrality) and manually distorted the geometry around a TM site to break symmetry and induce polaron formation at that particular site[26]. For a hole polaron in $\mathrm{LiFePO_4}$, we removed an electron and distorted the geometry in the opposite direction (i.e., we contracted the local $\mathrm{FeO_6}$ bonds). For structural relaxations, the PAW potential with the smallest radius was used except for $\mathrm{LiFePO_4}$ (see Table I), in which case the large core Fe potential was used due to issues described in the $\mathrm{LiFePO_4}$ results section. We calculated separate sets of structures for both DFT+U and HSE06. We performed polaron calculations in supercells deemed large enough to contain the defect, and all polaron hopping barriers were calculated by relaxing the transition state with the CI-NEB method[43]. A Gaussian smearing of 0.02 eV was used in all cases, but increased to 0.05 eV for displaying density of states (DOS) results. For rutile TiO_2, a $2 \times 2 \times 3$ supercell (24 formula units) was used for the polaron calculations with a $2 \times 2 \times 2$ Monkhorst-Pack k-point scheme. For Fe_2O_3, we used a supercell consisting of $2 \times 2 \times 1$ hexagonal unit cells (24 formula units), with only Γ-point sampling in the reciprocal space. A $1 \times 2 \times 2$ supercell (16 formula units) with Γ-point sampling was used for $FePO_4$ and $LiFePO_4$, and for spinel MnO_2 the cubic cell with 16 formula units was used with a $2 \times 2 \times 2$ Monkhorst-Pack k-point scheme. Values used for U_{eff} are 4.2 eV for TiO_2[32], 4.3 eV for FP/LFP[8] and Fe_2O_3[44], and 4.5 eV for MnO_2[45].

After relaxing all the required structures, we then calculated the properties with a set of PAW potentials supplied by VASP[16], of which the valencies and augmentation radii are listed in Table I. These include the standard potentials without semicore electrons (labeled "X"), potentials with $3p$ electrons (labeled "X_pv"), and potentials with $3s$ and $3p$ electrons (labeled "X_sv"). For Ti, we included an additional hard potential ("Ti_h") with an even smaller core radius. We also included the latest (2015) PAW potentials that are optimized for GW calculations (labeled "X_sv_GW") but are also seen as generally more accurate[46]. Results with these potentials might deviate slightly from the expected trends due to their different construction as they have more projectors and empty valence states.

The properties that we have studied are the band gap E_g, the polaron gap state E_p, the polaron formation energy E_{form}, and the bulk polaron hopping barrier (activation energy) E_a. We define the band gap $E_g = E_C - E_V$ as the difference between the conduction band minimum (CBM) and valence band maximum (VBM). We take the polaron gap state energy E_p relative to the CBM. The formation energy is calculated as the difference between the localized polaronic ground state and the initial, undistorted state $E_{\text{form}} = E_{\text{POL}} - E_{\text{INT}}$, and the activation energy E_a is the hopping barrier which is the difference between the transition state (TS) and ground state total energies $E_a = E_{\text{TS}} - E_{\text{POL}}$.

We verified the condition of linearity by varying the additional charge between 0 and 1 on a polaronic site using the polaronic ground state as our input structure[33,36]. For hole polarons in $LiFePO_4$, we varied this charge between -1 and 0. As these calculations are total energy comparisons, we applied corrections for the unphysical electrostatic interactions between the image charges of finite sized supercells[47,48].

For additional comparison, we also performed polaron hopping barrier E_a calculations with the plane-wave DFT code Abinit[49,50], using the same structures and parameters as in the VASP calculations. The DFT+U projection scheme in Abinit[51] differs slightly from the one used in VASP[19], leading to different calculated trends. For further details we refer to the supplemental material[52].

	Z_{val}	r_{PAW} (a.u.)
Ti	4	2.8
Ti_pv	10	2.5
Ti_sv	12	2.3
Ti_sv_GW	12	2.0
Ti_h	12	1.9
Mn	7	2.3
Mn_pv	13	2.3
Mn_sv_GW	15	2.0
Mn_sv	15	1.95
Fe	8	2.3
Fe_pv	14	2.2
Fe_sv_GW	16	2.0
Fe_sv	16	1.9

TABLE I. List of the potentials used in this study with their different valencies and PAW augmentation radii r_{PAW}. Other differences in PAW construction which are most notably between GW and non-GW potentials are not shown here.

IV. RESULTS

In this section we list our computed properties for each material (rutile TiO_2, Fe_2O_3, (Li)$FePO_4$, and spinel MnO_2) in its own subsection, comparing them to earlier calculations and experimental measurements if available. We also provide extensive analysis on the calculated trends in these materials, followed by a more in-depth analysis of the projection radius in Sec. V. We then recap our analysis and provide a general assessment of these trends in Sec. VI. Full datasets of our calculations are included in the supplemental material[52].

A. TiO_2

Titanium dioxide in its rutile form has a measured band gap of 3 eV[56]. Further experimental results[57] indicate a polaronic surface state in the band gap that is approximately 0.7 ± 0.1 eV below the CBM. While we cannot directly relate a surface state to one calculated in the bulk material, they still arise from the same physical origin of strong d-orbital correlations and we should be able to connect the two qualitatively.

From a chemical point of view, the Ti atoms are stripped of all their valence electrons leaving them in a d^0 state. This leads to TiO_2 being a strong CT insulator, with the valence band dominated by completely filled O $2p$ states, and the conduction band having Ti $3d$ character as shown in the projected DOS plot in Fig. 2. From this alone we can already argue that the DFT+U formalism should be insufficient as the U-term acts upon localized electrons with atomic-like d-character, of which there are formally none in this material. Its resulting ef-

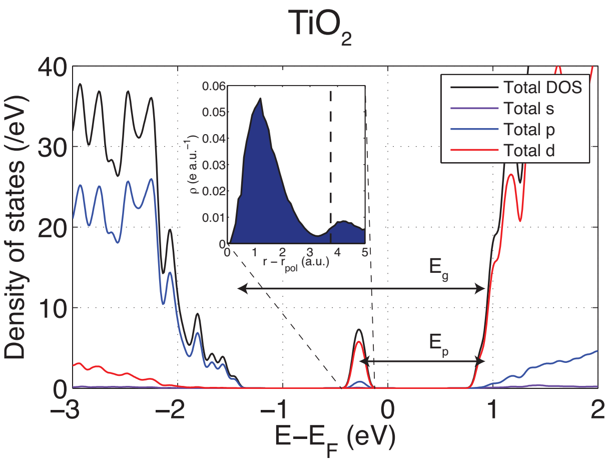

FIG. 2. (Color online) TiO_2 orbital projected DOS of the polaronic ground state. Inset: real space radial charge distribution of the polaronic state.

fect on the band gap should therefore be small, as has been calculated in previous DFT+U works[39,58]. As the projected $3d$ occupations inside the Ti spheres are still non-zero due to hybridization and non-orthogonality of other states entering the sphere (and can even be larger than 2 for large spheres[58]), the orbital dependent U-term will still act on these unphysical non-zero occupations, and this could lead to uncontrollable results[21]. We therefore expect that a hybrid functional such as HSE06 would fare better here as it is independent of both orbitals and their occupancies.

Fig. 2 shows the projected DOS of TiO_2, with one additional electron localized in a polaronic state. Calculations with DFT+U and HSE06 are qualitatively very similar, so we only show the DFT+U calculations here. The valence band consists entirely of p states, while the conduction band is fully d-like. The band gap E_g is defined as the energy difference between the lowest unoccupied state (CBM) and the highest occupied state (VBM), and the polaronic state E_p is defined relative to the CBM. According to the PDOS, this polaronic state is almost entirely of d-orbital character, which is also confirmed by the radial charge density plot in the inset of Fig. 2, showing behavior that is similar to an atomic $3d$ orbital.

Fig. 3 shows the band gap and polaron properties calculated with both DFT+U (U = 4.2 eV[32]) and HSE06 ($\alpha = 0.25$) methods while varying the Ti PAW potential. From the HSE06 plot in Fig. 3a which does not depend on projection radius, we see that the band gap incurs a slight increase with an increase in valence electrons (4 for $r_{\mathrm{PAW}} = 2.8$, 10 for $r_{\mathrm{PAW}} = 2.5$, and 12 for 4 for $r_{\mathrm{PAW}} \leq 2.3$). The different r_{PAW} of the three 12 electron potentials do not seem to affect the HSE06 results in any significant way. In comparison, the DFT+U plot in Fig. 3a shows a smaller increase of the gap with an increase in valence electrons, peaking at $r_{\mathrm{PAW}} = 2.3$ and then decreasing as we further decrease r_{PAW}. We can see that increasing the number of valence electrons has an effect similar to the HSE06 results, while there is an additional superimposed contribution from the different DFT+U projections, although it is not as drastic as the theory would suggest. We attribute this to the valence band being entirely of O $2p$ character, where the splitting from the DFT+U $3d$ projection has little effect. Furthermore, the increase in the number of semicore electrons leads to a slight increase of the gap, and the two effects somewhat cancel each other out. However, the position of the polaron state is influenced dramatically as seen in Fig. 3b. As r_{PAW} decreases, the distance between the polaron state and the CBM becomes smaller and smaller for DFT+U, while the HSE06 results are insensitive to the choice of r_{PAW}. This can be attributed to the DFT+U projection of the polaron state which is almost entirely of Ti $3d$ character and therefore is highly sensitive to the projection radius. Similar trends can be seen from the formation and activation energies in Fig. 3c and 3d, with the DFT+U results being highly sensitive to r_{PAW} and the HSE06 results being affected mostly by the difference in valence electrons, but relatively less so. From the DFT+U results in Fig. 3, we can see a relationship between the polaronic properties (formation and activation energies) and the position of the polaron within the band gap (vs. CBM). Qualitatively this makes sense, as the distance to the conduction band will determine how strong the self-trapping and hopping energies are.

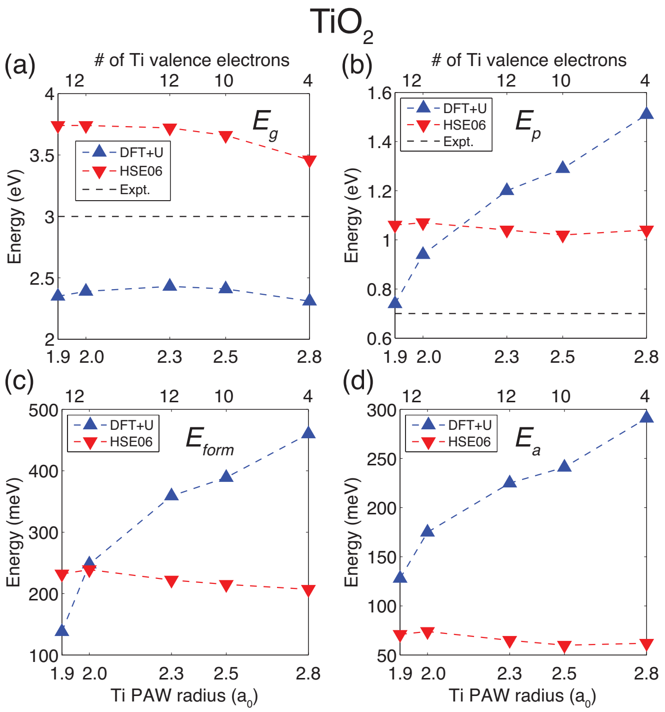

FIG. 3. (Color online) Calculated electronic properties of TiO_2 with DFT+U and HSE06 as a function of different PAW potentials. (a) band gap E_g, (b) polaronic gap state E_p, (c) formation energy E_{form}, (d) polaronic hopping barrier E_a.

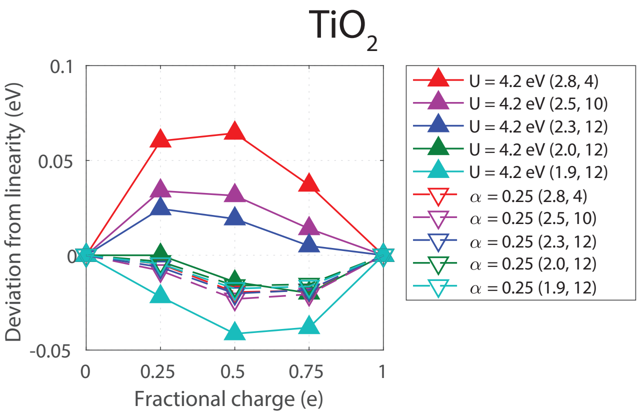

FIG. 4. (Color online) Deviation from linearity as a function of fractional charge in TiO_2. r_{PAW} and the number of valence electrons are listed for each PAW potential. $U = 4.2$ eV and $\alpha = 25\%$ in all DFT+U (solid upright triangles) and HSE06 (hollow inverted triangles) cases, respectively.

Fig. 4 shows the piecewise linearity in TiO_2 plotted with both DFT+U and HSE06. These results show the strong dependence of the calculated properties on r_{PAW} with DFT+U, in contrast to the weak dependence on semicore valence electrons of the calculated properties with HSE06. These results suggest a slightly increased α to be more consistent for HSE06 calculations, and either the $r_{PAW} = 2.3\ a_0$ or the $r_{PAW} = 2.0\ a_0$ potential to be the most consistent for DFT+U calculations in this material.

For TiO_2, it seems that HSE06 results are much more consistent as a function of varying PAW potential, and that there is a wide variance in our DFT+U results depending mainly on which projection radius is used. Combined with the unphysical behavior of DFT+U in d^0 materials, we conclude that HSE06 obtains more consistent results for TiO_2. Finally, comparing to experimental measurements, the HSE06 results for the band gap (expt. 3 eV) and polaron state (expt. 0.7 eV from CBM) seem to be about 0.6 eV and 0.3 eV off, respectively.

In order to improve the consistency of our prediction of the polaron hopping barrier, we can offer suggestions from two contrasting points of view. Firstly, it seems plausible to slightly reduce the mixing factor α to better match the band gap and polaron state with experimental results for TiO_2, thereby possibly improving the prediction of the hopping barrier. However, this suggestion is at variance if we consider the property of piecewise linearity (Fig. 4) that our functional needs to adhere to. To maintain consistency from the *ab initio* point of view, it is suggested rather to slightly increase α to maintain this piecewise linearity. As neither DFT+U nor HSE06 are exact functionals, we should not expect either of them to produce results that can be quantitatively compared to all measurable material properties.

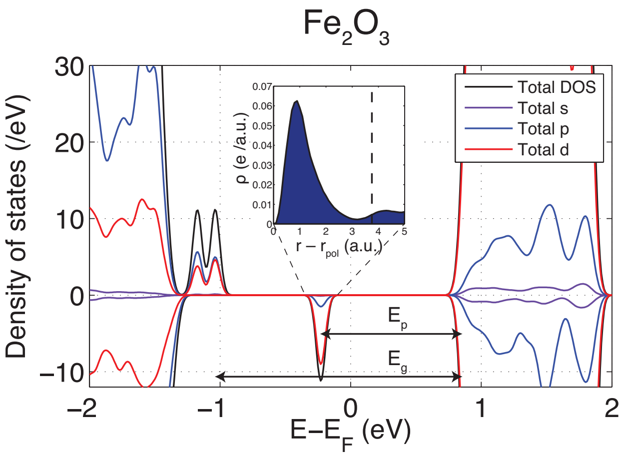

FIG. 5. (Color online) Fe_2O_3 orbital projected DOS of the polaronic ground state. Inset: real space radial charge distribution of the polaronic state.

B. Fe_2O_3 (Hematite)

For hematite, experimental data is available for three relevant characteristics, with the band gap measured at 2 eV[59], the polaron state with respect to the CBM at 0.7 eV[60], and the polaronic activation energy at 120 meV[60]. Additionally, the activation energy has been calculated at 130-150 meV in a previous DFT+U study[44], showing close correspondence to the experimental value. This makes hematite an ideal case to focus our computational study on.

Fig. 5 shows the projected DOS as well as the real space radial charge density plot of the polaronic state. As Fe^{3+} is in a high spin d^5 state, adding an extra electron will send it to the minority spin channel turning it into d^6 Fe^{2+}. The electronic properties in Fig. 6 show that DFT+U calculations with all potentials reproduce the band gap quite well, although the polaronic properties vary wildly per potential. These trends are quite comparable to the situation in TiO_2. The potential that achieves the best comparison of the activation barrier to experiment is the large core potential ($r_{PAW} = 2.3\ a_0$) with 8 valence electrons largely due to its larger projection radius, although the $r_{PAW} = 2.0\ a_0$ potential with 16 valence electrons comes closest to reproducing the polaron gap state.

In contrast to our TiO_2 results, the HSE06 method seems to fare worse in hematite compared to DFT+U. While the results are more consistent between different potentials and show expected trends with respect to semicore electrons, the standard mixing fraction of 25% overestimates the band gap to 3.5 eV in all cases as shown in Fig. 6a. When setting α to 12% to obtain a better band gap compared with experiment[61], we were unable to localize a polaron in Fe_2O_3, contrary to experimental evidence. The convex behavior shown in Fig. 7 corroborates these results. Using the standard $\alpha = 25\%$ for

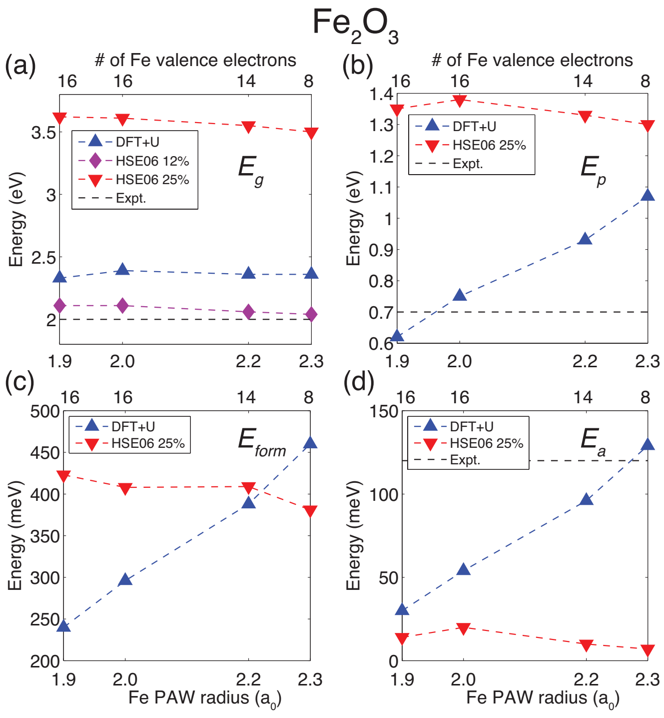

FIG. 6. (Color online) Calculated electronic properties of Fe_2O_3 with DFT+U and HSE06 using different PAW potentials. (a) band gap E_g, (b) polaronic gap state E_p, (c) formation energy $E_{\rm form}$, (d) polaronic hopping barrier E_a.

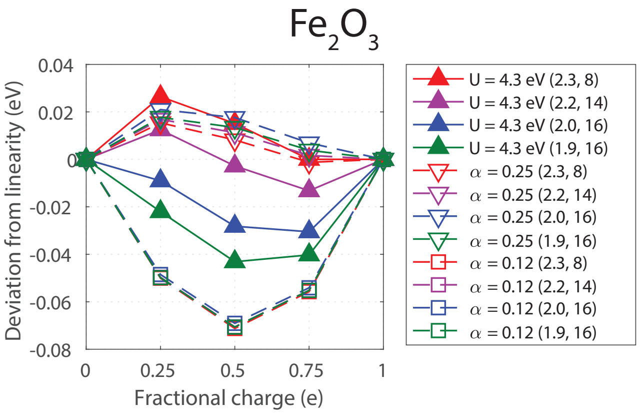

FIG. 7. (Color online) Deviation from linearity as a function of fractional charge in Fe_2O_3. $r_{\rm PAW}$ and the number of valence electrons are listed for each PAW potential. $U = 4.3$ eV in all DFT+U calculations (solid upright triangles), and the two sets of HSE06 calculations are done with $\alpha = 25\%$ (hollow inverted triangles) and $\alpha = 12\%$ (hollow squares).

polaron calculations which does allow polaron formation, we then obtained very low activation energies of 15 meV at $r_{\rm PAW} = 1.9\ a_0$, going down to almost 0 meV for the $r_{\rm PAW} = 2.3\ a_0$ potential. Therefore, it seems that for this material, DFT+U reproduces experimental results better, although careful attention is required concerning the projection radius.

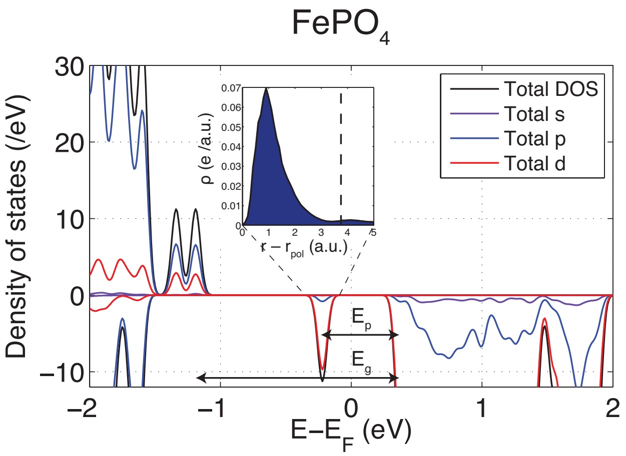

FIG. 8. (Color online) $FePO_4$ orbital projected DOS of the polaronic ground state. Inset: real space radial charge distribution of the polaronic state.

Fig. 7 shows the piecewise linearity calculations for both $\alpha = 25\%$ and $\alpha = 12\%$ in HSE06, as well as the DFT+U calculations. Once again, the HSE06 calculations are far more consistent compared to the DFT+U calculations with respect to $r_{\rm PAW}$. Here, we see the pitfall of choosing a parameter to fit the band gap[61], as choosing $\alpha = 12\%$ leads to a stronger underbinding compared to $\alpha = 25\%$ which results in a more consistent behavior for linearity in Fe_2O_3. For this material, the $r_{\rm PAW} = 2.2\ a_0$ potential seems the most consistent one for DFT+U, in contrast to the more accurate barrier calculated with the $r_{\rm PAW} = 2.3\ a_0$ potential compared to experiment[60].

C. $FePO_4$ and $LiFePO_4$ (LFP)

As it is challenging to synthesize a fully delithiated sample of $LiFePO_4$ ($FePO_4$), we will compare our results to a previous computational study[8,38], reproducing their results with the large core Fe potential ($r_{\rm PAW} = 2.3\ a_0$) while adding more insight by including the other potentials as well as the HSE06 method. Fig. 9 shows the results of this study, with all results following the trends as noted before; HSE06 results being dependent on mostly the number of electrons and DFT+U results showing a mostly downward trend with decreasing radius. The two main differences are that HSE06 calculations lead to a much larger band gap and a smaller polaron formation energy.

For $LiFePO_4$ in its fully lithiated phase, the experimental band gap has been measured at ~ 4 eV[7], while not much polaron information is available as the mobile Li^+ ions seem to form the rate limiting factor for conductivity measurements with their significantly higher diffusion barriers[8,62,63]. From the projected DOS in Fig. 10 we can see a significant qualitative difference between this material and the other materials studied. The Fe^{2+} peak is

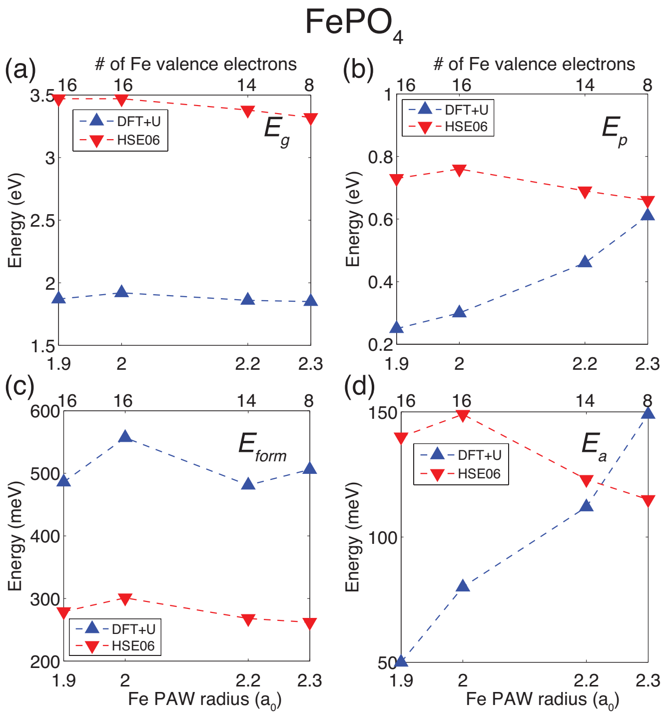

FIG. 9. (Color online) Calculated electronic properties of FePO$_4$ with DFT+U and HSE06 using different PAW potentials. (a) band gap E_g, (b) polaronic gap state E_p, (c) formation energy $E_{\rm form}$, (d) polaronic hopping barrier E_a.

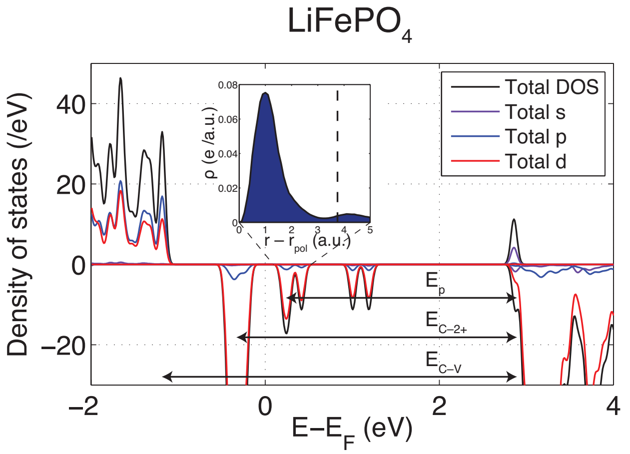

FIG. 10. (Color online) LiFePO$_4$ orbital projected DOS of the polaronic ground state. Inset: real space radial charge distribution of the polaronic state.

the highest occupied state, but it is localized and separated from the usual delocalized O $2p$ / Fe $3d$ hybridized valence band present in FePO$_4$ as shown in Fig. 8, making this material a true Mott-Hubbard insulator. From a FePO$_4$ perspective, LiFePO$_4$ could also be described as being fully saturated with polarons that are charge transferred from the Li$^+$ ions. We therefore have two definitions of a band gap in this material, depending on how we define this Fe^{2+} state. One definition is the delocalized CBM - delocalized VBM (labeled "CB - VB" in Fig. 11a), and the second one will be the traditional CBM - zero temperature E_F definition (labeled as "C - 2+" in Fig. 11a). We can see how the DFT+U projection comes into play for these two definitions in Fig. 11, with the "CB - VB" gap near constant and the traditional "CB - 2+" gap being strongly dependent on the potential used. This further clarifies our definition of the "2+" state as being polaron-like, as it is a pure Mott-Hubbard state and therefore highly sensitive to the projection radius. Furthermore, the empty hole polaron state above the Fermi energy retains the same position from both the CBM and the delocalized VBM. Thus, the only state that moves when changing the DFT+U projection radius is the 2+ state. For HSE06, both gaps remain unchanged which again shows that the polaron state is preserved in HSE regardless of which PAW radius we choose as shown in Fig. 11a. Here once again, HSE produces much more consistent gap states and barriers solely due to the fact that it is not dependent on a projection radius, although it again consistently calculates much higher band gaps.

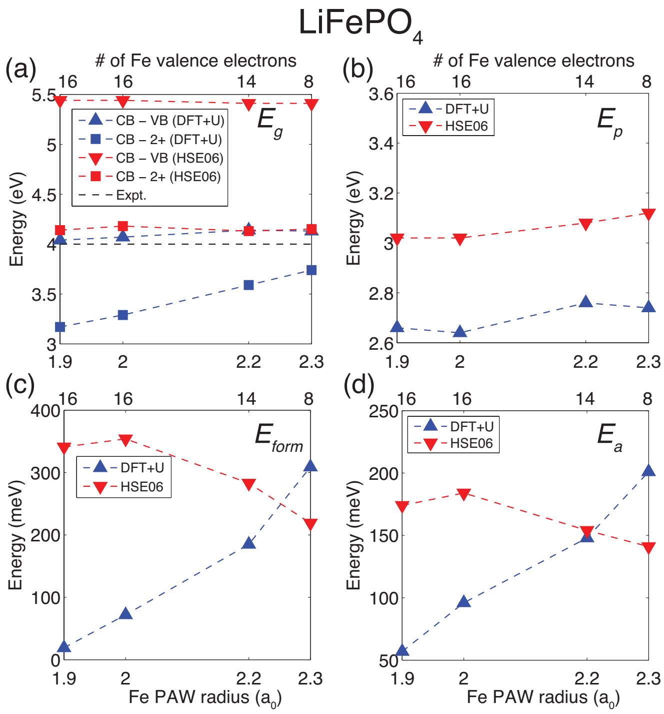

FIG. 11. (Color online) Calculated electronic properties of LiFePO$_4$ with DFT+U and HSE06 using different PAW potentials. (a) band gap E_g, (b) polaronic gap state E_p, (c) formation energy $E_{\rm form}$, (d) polaronic hopping barrier E_a.

Figs. 12 and 13 show our piecewise linearity calculations in FePO$_4$ and LiFePO$_4$. In both cases, both $U = 4.3$ eV and $\alpha = 25\%$ are too low to restore piecewise linearity in these materials. To maintain consistency within the respective methods, it therefore seems necessary to increase U and α regardless of potential used (see

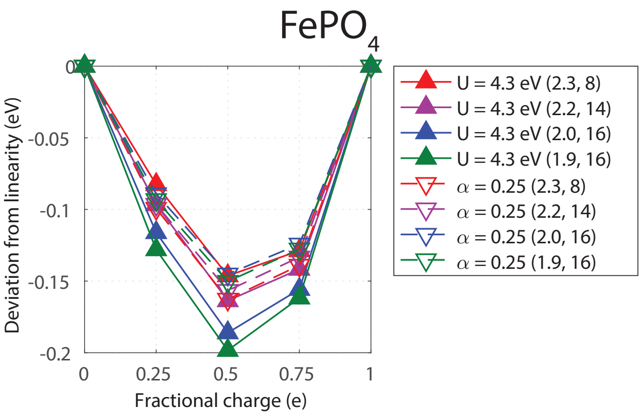

FIG. 12. (Color online) Deviation from linearity as a function of fractional charge in FePO$_4$. r_{PAW} and the number of valence electrons are listed for each PAW potential. $U = 4.3$ eV and $\alpha = 25\%$ in all DFT+U (solid upright triangles) and HSE06 (hollow inverted triangles) cases, respectively.

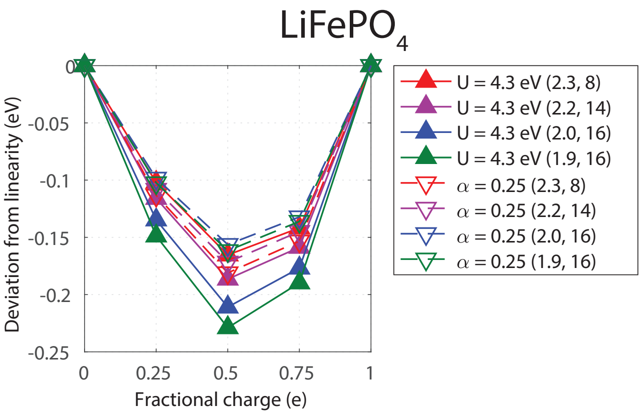

FIG. 13. (Color online) Deviation from linearity as a function of fractional charge in LiFePO$_4$. r_{PAW} and the number of valence electrons are listed for each PAW potential. $U = 4.3$ eV and $\alpha = 25\%$ in all DFT+U (solid upright triangles) and HSE06 (hollow inverted triangles) cases, respectively.

also the additional calculations in the supplemental material[52]).

The FePO$_4$ results are quite in line with the other materials. While LiFePO$_4$ is strongly Mott-Hubbard like, subsequently leading to stronger r_{PAW} effects in even the DFT+U calculated band gap. Also uniquely for LiFePO$_4$, we were unable to localize a hole polaron in DFT+U with the 16-electron small core potential ($r_{\mathrm{PAW}} = 1.9\ a_0$), and as such all structural calculations were done with the 8-electron, $r_{\mathrm{PAW}} = 2.3\ a_0$ potential. This can be clearly explained from the formation energy in Fig. 11, which becomes nearly zero (20 meV) as well as lower than the activation barrier as r_{PAW} is lowered. This 20 meV formation energy would lead to thermal excitations being able to easily delocalize the state, as well as band conduction being favored over hopping conduction as it would cost less energy to excite the electron into the conduction band. This shows once more the importance of setting a realistic projection radius, especially when calculating polaron properties.

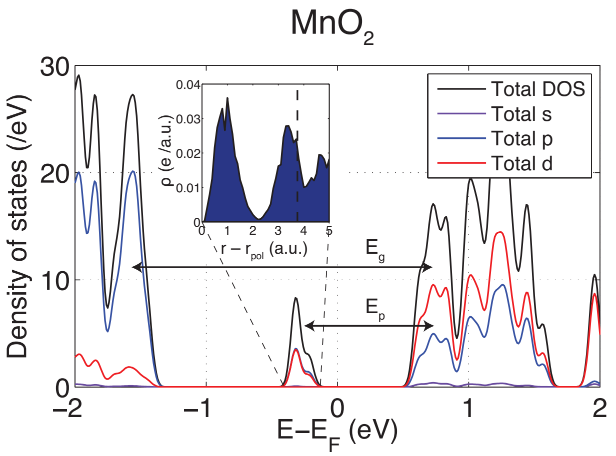

FIG. 14. (Color online) MnO$_2$ orbital projected DOS of the polaronic ground state. Inset: real space radial charge distribution of the polaronic state.

D. MnO$_2$

Band gap measurements have been done on LiMn$_2$O$_4$, which has half a Li for each formula unit of MnO$_2$. These additional Li atoms add electrons which relax further into polaronic states. Therefore, the measured d-d band gap of 1.2 eV[64] would correspond to the polaron gap state E_p as opposed to the Mn 3d - O 2p gap, which was measured to be around 3 eV[65] – this study also measured additional d-d transition energies of 1.63 eV and 2.00 eV. DFT+U calculations have been performed earlier[45] and have resulted in a calculated barrier of 0.22 eV for free polarons.

Fig. 14 shows the projected DOS for MnO$_2$ and its polaron real space radial density calculated in DFT+U. In contrast to the other materials studied, the MnO$_2$ projected DOS shows significant hybridization of the polaronic state, which is of approximately half p and half d character. This can also be clearly inferred from the inset, which shows a real space density that is shared between the Mn site and the O atoms, with a minimum at around 2.2 a_0. The physical implications of a more hybridized polaron state is that it is less sensitive to DFT+U parameters as it projects far less onto purely atomic d states. Additionally, the increased hybridization could be more general to other Mn-O compounds, where for example in MnPO$_4$ it was shown that DFT+U could not localize a polaron at all due to the increased hybridization[38].

The electronic properties of MnO$_2$ are shown in Fig. 15. At first glance, there are only quantitative differences between DFT+U and HSE06 here, with HSE06

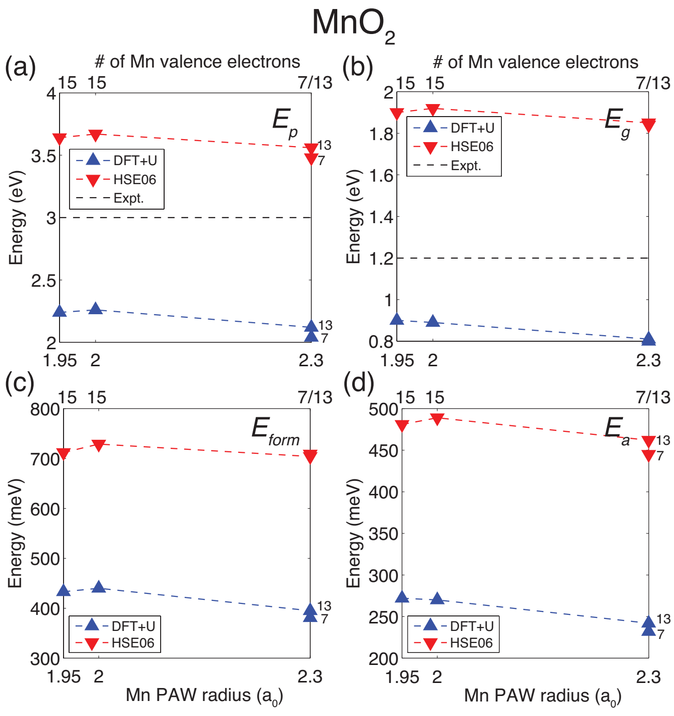

FIG. 15. (Color online) Calculated electronic properties of $\mathrm{MnO_2}$ with DFT+U and HSE06 using different PAW potentials. (a) band gap E_g, (b) polaronic gap state E_p, (c) formation energy E_{form}, (d) polaronic hopping barrier E_a.

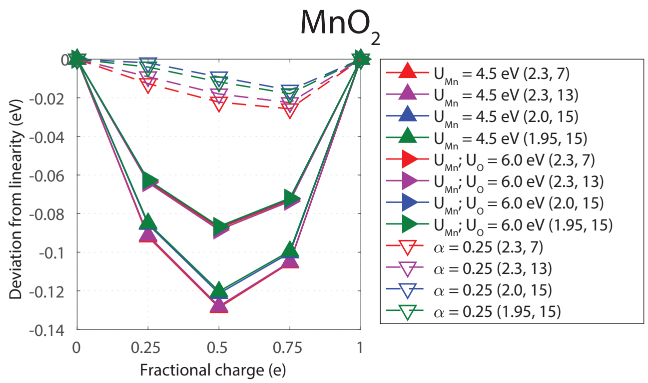

FIG. 16. (Color online) Deviation from linearity as a function of fractional charge in spinel $\mathrm{MnO_2}$. r_{PAW} and the number of valence electrons are listed for each PAW potential. $U_{\mathrm{Mn}} = 4.5$ eV and $\alpha = 25\%$ in all DFT+U (solid upright triangles) and HSE06 (hollow inverted triangles) calculations, respectively. We have included an additional set of calculations where we have set a $U_{\mathrm{O}} = 6.0$ eV on the O $2p$ states in addition to the existing $U_{\mathrm{Mn}} = 4.5$ eV (solid right facing triangles).

calculations resulting in higher energies over all projection radii. Both the 7-electron and 13-electron potential of Mn have the same radius of 2.3 au, allowing us to do a direct study of $3p$ semicore effects in Mn while keeping $\mathrm{r_{PAW}}$ the same. Those results are similar to the other materials, with more electrons leading to slightly higher energies. However, the DFT+U results are in contrast to the other materials, showing little effect of $\mathrm{r_{PAW}}$ and being qualitatively similar to the HSE06 results. The calculated activation energies E_a in Fig. 15d follow the same trend as the formation energies E_{form} and gap state energies E_p, showing relatively little dependence on r_{PAW}.

Fig. 16 shows the piecewise linearity in $\mathrm{MnO_2}$ calculated with both DFT+U ($U = 4.5$ eV) and HSE06. Consistent with the polaronic properties of Fig. 15, we show that linearity does not depend significantly on r_{PAW}, even for DFT+U calculations. While increasing the value of U increased concavity in all other materials studied (see supplemental material[52]), increasing it in $\mathrm{MnO_2}$ had little effect on linearity. However, applying a U_{O} on the O $2p$ states resulted in a better correction of the SIE for the TM-centered polaron in $\mathrm{MnO_2}$ and is likely due to the more hybridized polaronic state. This is again consistent with our earlier calculations suggesting that the strong hybridization in this material has lead to its properties being relatively unaffected by both U_{Mn} and r_{PAW}.

Thus, for spinel-type $\mathrm{MnO_2}$, DFT+U calculated properties depend very little on r_{PAW}. This is explained through two physical properties. Qualitatively, as shown in the projected DOS in Fig. 14, the $\mathrm{MnO_2}$ polaron state is strongly p-d hybridized and is therefore relatively insensitive to $\mathrm{r_{PAW}}$ in DFT+U, as there will be little projection onto atomic-like d states regardless of projection radius. Also, we can look at the real space density in Fig. 14 which drops to almost zero at around 2.2 a_0. This means that if we vary the projection radius between 1.95 and 2.3 a_0, the integrated value would likely vary little even if the state were of pure atomic $3d$ character.

V. DFT+U PROJECTION ANALYSIS

To study the effects arising from changing the projection radius, we plot the real space charge distribution of a polaronic state centered radially on its transition metal site in Fig. 17, taking $\mathrm{Fe_2O_3}$ as our case material. Polaron charge densities in the other materials are very similar as seen in the insets of the separate DOS figures so our analysis here will be general, with the exception of $\mathrm{MnO_2}$ which is treated separately due to its hybridization. The two black dashed lines represent the projection radius of the smallest core ($r_{\mathrm{PAW}} = 1.9\ a_0$) and the largest core ($r_{\mathrm{PAW}} = 2.3\ a_0$) PAW potential. The integrated charge density with $r_{\mathrm{PAW}} = 1.9\ a_0$ is 0.6698 compared to 0.7145 for $r_{\mathrm{PAW}} = 2.3\ a_0$, leading to a difference in projection of approximately 0.05 electrons. We can see that both radii are approximate as they are both relatively far up the tail and neither projection encompasses even 90% of the electron density. For half an electron on a TM site in the $\mathrm{Fe_2O_3}$ "TS" state, these numbers are 0.3481 and 0.3749 respectively, a difference of approximately 0.025 electrons.

The magnitude of these differences directly influences

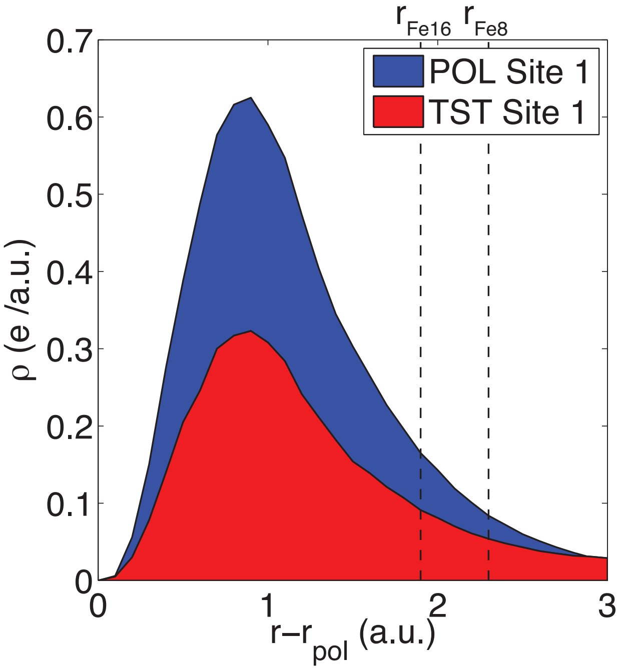

FIG. 17. (Color online) Real space radial charge distribution around a polaronic Fe site in Fe_2O_3. The blue curve and area corresponds to the polaronic ground state ("POL"). The red curve and area corresponds to the transition state ("TS"), where half of the electron density is centered on this site and the other half is centered on a neighboring site. The PAW radii shown correspond to the large ($r_{\mathrm{PAW}} = 2.3a_0$, 8 valence electrons) and small core Fe ($r_{\mathrm{PAW}} = 1.9a_0$, 16 valence electrons) potentials.

the energy term of Eq. (1) and affects the *d*-*d* splitting as seen in the differences of the locations of the polaron gap states for all the materials studied including Fe_2O_3, as well as the CBM - VBM gap in $LiFePO_4$. For the formation and activation energies, the effect is more subtle as it relies on an energy difference between the U-term energy contributions. However, in both cases this can be traced back to the quadratic dependence on the occupancy of the U-term. We first rewrite Eq. (1) as a sum of on-site U-term energy contributions:

$$E_{\mathrm{DFT+U}} = E_{\mathrm{DFT}} + E^U \equiv E_{\mathrm{DFT}} + \sum_t E_t^U(N), \qquad (5)$$

where the sum goes over all sites t, and N is the (projected) occupancy of local electrons at site t. The activation energy $E_a = E_{\mathrm{TS}} - E_{\mathrm{POL}}$ is defined as the total energy difference between the transition state configuration ("TS") where the electron is shared between two neighboring sites (labeled t^A and t^B) and the polaronic ground state configuration ("POL") where the electron is localized on one site (labeled t^A) only. Focusing on the projection-dependent U-term contributions and separating out the other terms (that we assume depend negligibly on the projection), we rewrite E_a as:

$$E_a = E_{\mathrm{TS}} - E_{\mathrm{POL}} = E_{\mathrm{TS}}^U - E_{\mathrm{POL}}^U + \Delta E_{\mathrm{other}}, \qquad (6)$$

$$E_{\mathrm{POL}}^U = E_{t^A}^U(N+1) + \sum_{t \neq t^A} E_t^U(N), \qquad (7)$$

$$E_{\mathrm{TS}}^U = E_{t^A}^U(N+1/2) + E_{t^B}^U(N+1/2) + \sum_{t \neq t^A, t^B} E_t^U(N). \qquad (8)$$

To first order $E_{t^A}^U(N+1/2) = E_{t^B}^U(N+1/2) = E_t^U(N+1/2)$ and assuming that, in a linear approximation, we can write $E_t^U(N+x) \approx E_t^U(N) + E_t^U(x)$, the relevant U-term energy difference becomes

$$E_a^U \approx 2E_t^U(1e/2) - E_t^U(1e), \qquad (9)$$

as all other on-site differences within $E_{t,\mathrm{TS}}^U(N) - E_{t,\mathrm{POL}}^U(N)$ are approximately zero. Fundamentally, this is the difference between the on-site energy of two half polarons and one whole polaron. As the energy terms are quadratically dependent on the projected charge (see Eq. (1)), changing this projection will lead to a change in this energy difference, as seen in our calculations. The argument for the formation energy follows in a similar fashion, with the higher energy configuration in this case being the intrinsic, delocalized solution which has the relevant energy difference of

$$E_{\mathrm{form}}^U = nE_t^U(e/n) - E_t^U(1e), \qquad (10)$$

where n is the number of polaronic sites (which is equal to the number of TM sites) in a supercell calculation. When the projection radius changes, the amount of charge ascribed to $+U$ interactions varies from the idealized fractions presented in the above equations. Since the $+U$ is correction is quadratic with the total number of projected electrons, this often leads to a particularly acute polaronic energy dependence on the projection radius that is manifest in nearly all polaronic properties (the major exception being MnO_2, which projects far less onto d-states, as discussed in the previous section).

VI. DISCUSSION

We have calculated four different electronic properties in five different materials. Not only have we calculated the band gap, we have also studied the three additional polaronic properties of these materials. From these results, we can establish a few trends as well as understand cases where these trends do not seem to hold. First of all, from our HSE06 calculations, we can see that in almost all cases, including semicore electrons leads to a band gap widening of up to 0.3 eV, and an increase in the activation energy of up to 30 meV. Formation energies can increase by up to 0.1 eV in $LiFePO_4$, but are relatively flat in the other cases. The polaron state is similarly unchanged in HSE06 calculations. We can then eliminate the variable of semicore electrons by comparing these results with our DFT+U calculations. Assuming that these effects are similar for both HSE06 and DFT+U calculations, we can begin to understand the effects of changing r_{PAW} on our DFT+U results. The general trend seems to be that all investigated polaron properties (E_p, E_{form}, and E_a), for sufficiently atomic-like polaron states (this excludes Mn_2O_4), decrease in magnitude with decreasing r_{PAW} when the DFT+U method is employed (in a manner that is dependent on r_{PAW}). *This trend is much less observable in the calculated band gaps, and using the band gap as sole criterion for fitting U therefore does not seem sufficient for calculations predicting polaronic properties.*

The band gap (with the important exception of $LiFePO_4$ as shown in Fig. 11a) remains relatively flat when varying r_{PAW}, and our results indicate that this arises from a cancellation of errors. Adding semicore electrons will increase the gap, but the simultaneous decrease of r_{PAW} leads to less projected on-site charge and therefore a smaller d-d separation. The decrease in the band gap is not as dramatic as one would expect from the projection onto r_{PAW}, as the occupied d states are typically far below E_F leading to an O 2p dominated valence band which is more CT-like in behavior. The important exception to this is $LiFePO_4$, whose VBM is strongly localized and d-like. In that case we can clearly see the effect of changing r_{PAW} on the d-d separation, as the HSE06 results remain flat here as well.

The three polaronic properties (E_p, E_{form}, and E_a) show remarkably similar behavior and trends, and unlike the band gap E_g, all depend strongly on the potential being used, with MnO_2 being the exception. The energy of the polaron state inside the band gap E_p is a better measure of the effects of changing r_{PAW}, as it is localized and strongly d-like, while relatively unaffected by semicore interactions. This is where we can see the clearest trends in all materials, except for MnO_2, with E_p depending monotonically on r_{PAW}. The polaron state in MnO_2 is much more hybridized with neighboring O 2p orbitals and is therefore largely unaffected by the projection onto pure 3d atomic orbitals as shown in Fig 15. This is an important property as polaron gap states can be experimentally measured, giving perhaps a better benchmark to fit the value of U on as the d-d character is more consistent with the spirit of DFT+U compared to the band gap which in many cases is more CT-like.

The formation and activation energies E_{form} and E_a are more direct indicators of polaron dynamics in a material. Here again, the DFT+U values are highly dependent on r_{PAW}, while the HSE06 results are much flatter. As energies calculated here have an exponential effect on the predicted dynamics, it raises a clear ambiguity for DFT+U results. Which potential is the one that we can trust? The best current comparison to experiment is hematite[60], where the activation energy calculated with the Fe potential with 8 valence electrons and $r_{\mathrm{PAW}} = 2.3\ a_0$ comes closest to reproducing the measured value of 130-150 meV (see Fig. 6d). This is at variance with the traditional guidelines of smaller core and more electrons always leading to better results. Another example, related to the formation energy, is seen in $LiFePO_4$, where we were only able to localize a polaron with the large core Fe potential ($r_{\mathrm{PAW}} = 2.3\ a_0$). Further analysis showed the reason behind this; the formation energy decreased sharply with decreasing r_{PAW} with the smallest core ($r_{\mathrm{PAW}} = 1.9\ a_0$) having a formation energy of 20 meV. This not only lead to computational issues in finding such a shallow energy well, but, being lower than the activation energy, also lead to the qualitatively erroneous prediction that the hole polaron preferred delocalized band conduction over hopping.

Our linearity calculations show similar differences between DFT+U and HSE06; the results for different r_{PAW} vary wildly in DFT+U whereas HSE06 calculations are more consistent, with semicore electrons having a far weaker influence when they are the only variable considered. This confirms that the projection radius affects calculated polaronic properties through a fundamental change in self interaction behavior. As these results imply that the value of U and the projection radius are co-dependent, a future study could compare results with a different U chosen for each projection radius in a consistent manner such that piecewise linearity is preserved for each potential. We believe that such a study could lead to a more consistent prediction of polaronic properties across the board.

Lastly, we have found that the implementation of the on-site projection in Abinit[51] differs slightly from the implementation in VASP[19]: the projector function in Abinit is a ground state atomic orbital[51] whereas the crystal wave function is projected onto spherical harmonics in VASP[19]. The Abinit results (see supplemental material in Ref.[52]) appear to show less potential dependent variation, and we suggest that the rapidly decaying d and f atomic orbitals beyond $r \sim 1.5$ Å are the underlying cause. However, further potential database development is required to verify such improvements.

VII. CONCLUSION

We have conducted an extensive study on the calculation of polaronic properties in several materials (rutile TiO_2, Fe_2O_3, $FePO_4$/$LiFePO_4$, and spinel MnO_2) with both DFT+U and HSE06 methods. We have studied the influence of both semicore electrons and projection radii on the calculated band gaps, polaron gap states, formation energies, and activation energies by varying the PAW potential for the transition metal, and have shown that the HSE06 method in almost all cases is more robust and more consistent (when the DFT+U PAW implementation depends on r_{PAW}). However, HSE06 does not give universally better results compared to the DFT+U method. While being more consistent, the drawback of hybrid functionals is the one to two orders of magnitude higher computational expense, making DFT+U methods still a very realistic approach to studying polaronic properties.

Our calculations have shown that semicore electrons have a small effect on polaronic properties, increasing the calculated band gap by up to 0.3 eV, and activation energies by up to 30 meV. The effects of different projection radii on DFT+U calculations are, apart from the band gap, dramatically more significant. This directly arises from the U-term energy contribution which is quadratically dependent on the locally projected density matrix, and we believe that, since the band gap remains often relatively unaffected due to reasons discussed in this work, the impact of the projection radius on other properties is not generally emphasized in the literature. Fundamentally, we have shown (see also the supplemental material[52]) that the projection radius changes the self interaction corrective properties of DFT+U, leading to a dependency of U on the projection radius. In particular, when studying polaronic properties with the DFT+U method, extensive care must be taken to remain consistent with not only the band gap but also properties such as the gap state, while taking the projection radius into account as an additional variable apart from the value for U. In general, one may extend these insights to other Mott-Hubbard influenced properties as well, as they might also be impacted if the projection radius were inconsistent between comparative DFT+U calculations.

To further progress in the analysis of polaronic properties predicted, more experimental measurements of polaron activation energies and gap state positions are needed. As polaronic properties are one of the factors determining the performance of energy and catalytic materials, having consistency in first principles calculations allows us to better compare them with measured values, as well as make more confident predictions in novel materials. Future work should focus on coupling theory and experiment in this manner.

ACKNOWLEDGMENTS

Z.W., A.M., and K.H.B. acknowledge financial support from Mitacs, Hydro-Québec, and NSERC, and computational support from Compute Canada and Calcul Québec. C.B. acknowledges support from the US NSF IRES-1261117 and NSF CBET-1403456. Z.W. would like to thank Vladimir Timoshevskii for insightful discussions on DFT+U theory.

---

[*] zi.wang3@mail.mcgill.ca

[1] A. K. Padhi, K. Nanjundaswamy, and J. B. Goodenough, J. Electrochem. Soc **144**, 1188 (1997).
[2] S. C. Warren, K. Voïtchovsky, H. Dotan, C. M. Leroy, M. Cornuz, F. Stellacci, C. Hébert, A. Rothschild, and M. Grätzel, Nature Mater. **12**, 842 (2013).
[3] E. W. McFarland and H. Metiu, Chem. Rev. **113**, 4391 (2013).
[4] T. Holstein, Ann. Phys **8**, 325 (1959).
[5] V. I. Anisimov, F. Aryasetiawan, and A. I. Lichtenstein, J. Phys. Condens. Matter **9**, 767 (1997).
[6] C. Adamo and V. Barone, J. Chem. Phys. **110**, 6158 (1999).
[7] F. Zhou, K. Kang, T. Maxisch, G. Ceder, and D. Morgan, Solid State Commun. **132**, 181 (2004).
[8] T. Maxisch, F. Zhou, and G. Ceder, Phys. Rev. B **73**, 104301 (2006).
[9] V.I. Anisimov and O. Gunnarsson, Phys. Rev. B **43**, 7570 (1991).
[10] V.I. Anisimov, J. Zaanen, and O.K. Andersen, Phys. Rev. B **44**, 943 (1991).
[11] A.I. Liechtenstein, V.I. Anisimov, and J. Zaanen, Phys. Rev. B **52**, R5467 (1995).
[12] G. Madsen and P. Novák, Europhys. Lett. (2005).
[13] M. Cococcioni and S. de Gironcoli, Phys. Rev. B **71**, 035105 (2005).
[14] J. P. Perdew and A. Zunger, Physical Review B **23**, 5048 (1981).
[15] J. P. Perdew, R. G. Parr, M. Levy, and J. L. Balduz Jr, Physical Review Letters **49**, 1691 (1982).
[16] G. Kresse and D. Joubert, Phys. Rev. B **59**, 1758 (1999).
[17] P. E. Blöchl, Phys. Rev. B **50**, 17953 (1994).
[18] J. Paier, R. Hirschl, M. Marsman, and G. Kresse, J. Chem. Phys. **122**, 234102 (2005).
[19] O. Bengone, M. Alouani, P. Blöchl, and J. Hugel, Phys. Rev. B **62**, 16392 (2000).
[20] C. Loschen, J. Carrasco, K. M. Neyman, and F. Illas, Phys. Rev. B **75**, 035115 (2007).
[21] S. Fabris, S. de Gironcoli, S. Baroni, G. Vicario, and G. Balducci, Phys. Rev. B **71**, 041102 (2005).
[22] W. E. Pickett, S. C. Erwin, and E. C. Ethridge, Phys. Rev. B **58**, 1201 (1998).
[23] A. K. McMahan, R. M. Martin, and S. Satpathy, Phys. Rev. B **38**, 6650 (1988).
[24] M. Ni, M. K. Leung, D. Y. Leung, and K. Sumathy, Renew. Sustainable Energy Rev. **11**, 401 (2007).
[25] L. Charette, J. Adams, M. Gaffey, T. McCord, et al., J. Geophys. Res **89**, 6899 (1984).
[26] Z. Wang and K. H. Bevan, Phys. Rev. B **93**, 024303 (2016).
[27] A. V. Krukau, O. A. Vydrov, A. F. Izmaylov, and G. E. Scuseria, J. Chem. Phys. **125**, 224106 (2006).
[28] S. L. Dudarev, G. A. Botton, S. Y. Savrasov, C. J. Humphreys, and A. P. Sutton, Phys. Rev. B **57**, 1505 (1998).
[29] I.V. Solovyev, P.H. Dederichs, and V.I. Anisimov, Phys. Rev. B **50**, 16861 (1994).
[30] A. B. Shick, A. I. Liechtenstein, and W. E. Pickett, Phys. Rev. B **60**, 10763 (1999).
[31] A. Rohrbach, J. Hafner, and G. Kresse, J. Phys. Condens. Matter **15**, 979 (2003).
[32] B. J. Morgan and G. W. Watson, J. Phys. Chem. C **113**, 7322 (2009).
[33] S. Lany and A. Zunger, Physical Review B **80**, 085202 (2009).

[34] A. R. Nagaraja, N. H. Perry, T. O. Mason, Y. Tang, M. Grayson, T. R. Paudel, S. Lany, and A. Zunger, Journal of the American Ceramic Society **95**, 269 (2012).

[35] P. R. Keating, D. O. Scanlon, B. J. Morgan, N. M. Galea, and G. W. Watson, The Journal of Physical Chemistry C **116**, 2443 (2012).

[36] P. Erhart, A. Klein, D. Åberg, and B. Sadigh, Phys. Rev. B **90**, 035204 (2014).

[37] A. Lindman, P. Erhart, and G. Wahnström, Physical Review B **94**, 075204 (2016).

[38] S. P. Ong, V. L. Chevrier, and G. Ceder, Phys. Rev. B **83**, 075112 (2011).

[39] T. Shibuya, K. Yasuoka, S. Mirbt, and B. Sanyal, J. Phys. Condens. Matter **24**, 435504 (2012).

[40] V. Ivády, R. Armiento, K. Szász, E. Janzén, A. Gali, and I. A. Abrikosov, Phys. Rev. B **90**, 035146 (2014).

[41] G. Kresse and J. Hafner, Phys. Rev. B **47**, 558 (1993); **49**, 14251 (1994); G. Kresse and J. Furthmüller, Comput. Mater. Sci. **6**, 15 (1996); G. Kresse and J. Furthmüller, Phys. Rev. B **54**, 11169 (1996).

[42] J. P. Perdew, K. Burke, and M. Ernzerhof, Phys. Rev. Lett. **77**, 3865 (1996); **78**, 1396 (1997).

[43] G. Henkelman, B. P. Uberuaga, and H. Jónsson, J. Chem. Phys **113**, 9901 (2000).

[44] N. Adelstein, J. B. Neaton, M. Asta, and L. C. De Jonghe, Phys. Rev. B **89**, 245115 (2014).

[45] C. Ouyang, Y. Du, S. Shi, and M. Lei, Phys. Lett. A **373**, 2796 (2009).

[46] K. Lejaeghere et al., Science **351**, aad3000 (2016).

[47] G. Makov and M.C. Payne, Physical Review B **51**, 4014 (1995).

[48] S. Lany and A. Zunger, Physical Review B **78**, 235104 (2008).

[49] X. Gonze et al., Comput. Phys. Commun. **180**, 2582 (2009).

[50] M. Torrent, F. Jollet, F. Bottin, G. Zérah, and X. Gonze, Comput. Mater. Sci **42**, 337 (2008).

[51] B. Amadon, F. Jollet, and M. Torrent, Phys. Rev. B **77**, 155104 (2008).

[52] See supplemental material at [url will be inserted by publisher] for full calculation datasets and supplemental Abinit calculations, which includes Refs.[53–55].

[53] F. Jollet, M. Torrent, and N. Holzwarth, Comput. Phys. Commun. **185**, 1246 (2014).

[54] N. Holzwarth et al., "Periodic Table of the Elements for PAW Functions (<2013),".

[55] N. Holzwarth, A. Tackett, and G. Matthews, Comput. Phys. Commun. **135**, 329 (2001).

[56] D. C. Cronemeyer, Phys. Rev. **87**, 876 (1952).

[57] M. Setvin, C. Franchini, X. Hao, M. Schmid, A. Janotti, M. Kaltak, C. G. Van de Walle, G. Kresse, and U. Diebold, Phys. Rev. Lett. **113**, 086402 (2014).

[58] N.A. Deskins and M. Dupuis, Phys. Rev. B **75**, 195212 (2007).

[59] S. Mochizuki, Phys. Status Solidi (a) **41**, 591 (1977).

[60] S. Chatman, C. I. Pearce, and K. M. Rosso, Chem. Mater. **27**, 1665 (2015).

[61] Z. D. Pozun and G. Henkelman, J. Chem. Phys. **134**, 224706 (2011).

[62] B. Ellis, L. K. Perry, D. H. Ryan, and L. Nazar, J. Am. Chem. Soc **128**, 11416 (2006).

[63] A. Mascaro, Z. Wang, P. Hovington, Y. Miyahara, A. Paolella, V. Gariepy, Z. Feng, T. Enright, C. Aiken, K. Zaghib, et al., "Measuring spatially resolved collective ionic transport on lithium battery cathodes using atomic force microscopy," (2017).

[64] C. Ouyang, H. Deng, Z. Ye, M. Lei, and L. Chen, Thin Solid Films **503**, 268 (2006).

[65] K. Kushida and K. Kuriyama, Appl. Phys. Lett. **77**, 4154 (2000).